nanomaterials

MDPI

Article

Magnetic Attributes of $NiFe_2O_4$ Nanoparticles: Influence of Dysprosium Ions (Dy^{3+}) Substitution

Munirah Abdullah Almessiere [1,2,*], Y. Slimani [1,*], H. Güngüneş [3], S. Ali [4], A. Manikandan [5], I. Ercan [1], A. Baykal [6] and A.V. Trukhanov [7,8,9]

1 Department of Biophysics, Institute for Research & Medical Consultations (IRMC), Imam Abdulrahman Bin Faisal University, P.O. Box 1982, Dammam 31441, Saudi Arabia; iercan@iau.edu.sa
2 Department of Physics, College of Science, Imam Abdulrahman Bin Faisal University, P.O. Box 1982, Dammam 31441, Saudi Arabia
3 Department of Physics, Hitit University, Çevre Yolu Bulvarı-Çorum 19030, Turkey; gungunes@gmail.com
4 Mechanical and Energy Engineering Department College of Engineering, Imam Abdulrahman bin Faisal University, P.O. Box 1982, Dammam 31441, Saudi Arabia; sadali@iau.edu.sa
5 Department of Chemistry, Bharath Institute of Higher Education and Research, Bharath University, Chennai, Tamil Nadu 600073, India; manikandana.che@bharatuniv.ac.in
6 Department of Nano-Medicine Research, Institute for Research & Medical Consultations (IRMC), Imam Abdulrahman Bin Faisal University, P.O. Box 1982, Dammam 31441, Saudi Arabia; abaykal@iau.edu.sa
7 Scientific-Practical Materials Research Centre NAS of Belarus, 19 P. Brovki Street, 220072 Minsk, Belarus; truhanov86@mail.ru
8 Department of Electronic Materials Technology, National University of Science and Technology MISiS, Leninsky Prospekt, 4, Moscow 119049, Russia
9 Laboratory of Crystal Growth, South Ural State University, Lenin Prospect, 76, Chelyabinsk 454080, Russia
* Correspondence: malmessiere@iau.edu.sa (M.A.A.); yaslimani@iau.edu.sa (Y.S.); Tel.: +966-50-580-7292 (M.A.A.); +966-59-965-8876 (Y.S.)

Received: 2 May 2019; Accepted: 28 May 2019; Published: 31 May 2019

Abstract: This paper reports the influence of dysprosium ion (Dy^{3+}) substitution on the structural and magnetic properties of $NiDy_xFe_{2-x}O_4$ ($0.0 \leq x \leq 0.1$) nanoparticles (NPs) prepared using a hydrothermal method. The structure and morphology of the as-synthesized NPs were characterized via X-ray diffraction (XRD), scanning and transmission electron microscope (SEM, and TEM) analyses. ^{57}Fe Mössbauer spectra were recorded to determine the Dy^{3+} content dependent variation in the line width, isomer shift, quadrupole splitting, and hyperfine magnetic fields. Furthermore, the magnetic properties of the prepared NPs were also investigated by zero-field cooled (ZFC) and field cooled (FC) magnetizations and AC susceptibility measurements. The M_{ZFC} (T) results showed a blocking temperature (T_B). Below T_B, the products behave as ferromagnetic (FM) and act superparamagnetic (SPM) above T_B. The M_{FC} (T) curves indicated the existence of super-spin glass (SSG) behavior below T_s (spin-glass freezing temperature). The AC susceptibility measurements confirmed the existence of the two transition temperatures (i.e., T_B and T_s). Numerous models, e.g., Neel–Arrhenius (N–A), Vogel–Fulcher (V–F), and critical slowing down (CSD), were used to investigate the dynamics of the systems. It was found that the Dy substitution enhanced the magnetic interactions.

Keywords: $NiFe_2O_4$; spinel ferrites; structure; microstructure; magnetization; AC susceptibility

1. Introduction

Lately, nanosized Ni-spinel ferrites have widely been used in magnetic storage media, magnetic adsorbents, telecommunication, catalysts, microwave absorbers, and computer memories [1–5]. Further, the structural and magnetic characteristics of nanosized Ni-spinel ferrites have been enhanced

by substituting varieties of magnetic, nonmagnetic, and rare earths ions [6–8]. Such improvement was majorly attributed to the distribution of substitution ions between tetrahedral and octahedral sites of the host and eventual influence on their magnetic moments [8]. Moreover, the use of rare earths as substitution agents in the spinel ferrite was found to cause structural distortion through symmetry preserving the lattice strain and thereby modifying the overall properties of nanosized spinel ferrites [9]. Intense research efforts have been made to enhance the structure, optical, and magnetic properties of rare earth ion substituted nanosized Ni-spinel ferrites [2,3]. Meanwhile, different theories and models have been applied to achieve a better understanding of the unique magnetic properties of these doped nanosized Ni-spinel ferrites [2,3]. Modified magnetic properties of Erbium (Er^{3+}) and Samarium (Sm^{3+}) substituted nickel ferrites were analyzed by low temperature magnetization, and zero-field cooled and field cooled (ZFC-FC) measurements. Such samples revealed a superparamagnetic (SPM) behavior with very low coercivity (H_c) and remanence magnetization (M_r), making them suitable for developing soft magnets [10]. A substitution of Pr, Sm, and La in $Ni_{0.5}Zn_{0.5}Fe_{1.95}R_{0.05}O_4$ nanoparticles (NPs) was found to modify their magnetic and dielectric properties [11]. Conversely, Cerium (Ce) substituted Ni-Zn at low contents ($0.0 \leq x \leq 0.1$) produced high saturation magnetization (M_s), remanence, and coercivity [12].

So far, studies on Dy^{3+} substituted nanosized Ni spinel ferrites are rare. J. Sahariya et al. [13] reported the temperature dependent spin momentum densities of $NiFe_{2-x}RE_xO_4$ ($x = 0$, 0.05 and RE = Dy, Gd) ferrites measured by using a magnetic Compton spectrometer. The experimental profiles of $NiFe_2O_4$ with doping of Dy and Gd show a similar spin moment to the non-doped sample. The contribution of different constituents in the formation of total spin moment is deduced from the analysis of the Compton line shape. It is seen that Dy^{3+} or Gd^{3+} doping ions at Fe^{3+} sites lead to a redistribution of the spin moment at Fe^{3+} and RE^{3+} sites. The temperature dependent magnetic Compton profiles are decomposed into the constituent profiles of Ni, Fe, Dy/Gd, and diffuse components, arising due to O-2sp states. A decrease in the Fe spin moment from 0.55 ± 0.03 μ_B/f.u. (in $NiFe_2O_4$) to 0.41(0.50) ± 0.03 μ_B/f.u. is observed on the partial substitution of Dy(Gd). K. Kamala Bharathi et al. [14] reported a correlation between the microstructure, electrical, and optical properties of Dysprosium-doped nickel-ferrite ($NiFe_{1.925}Dy_{0.075}O_4$) thin films fabricated using sputter-deposition using a stoichiometric bulk target prepared by tsolid-state chemical reaction. Recently, M.A. Almessiere et al. [15] investigated the effects of dysprosium substitution on the structural, microstructural, and magnetic properties of $NiFe_2O_4$ nanoparticles. The formation of the cubic phase of Ni nanosized ferrites was confirmed. The magnetic properties were done by analyzing measurements of the magnetization versus applied field M(H). These measurements were carried out at two different temperatures—room temperature (T = 300 K) and low temperature (T = 10 K). A noticeable improvement in the differently deduced magnetic parameters, including saturation magnetization (M_s), remanence (M_r), and coercivity (H_c), was observed at both room (T = 300 K) and low (T = 10 K) temperatures with Dy substitution. The increase in the different magnetic parameters is mainly attributed to the strengthening of A–B exchange interactions owing to the substitution of Fe^{3+} ions with Dy^{3+} ions with larger ionic radii, the formation of local strains, and the increase in the magnetic moments (N_B).

To the best of our knowledge, there is no study reporting the Mossbauer, zero-field cooled (ZFC), and field cooled (FC) magnetizations and AC susceptibility measurements for Dy substituted nanoparticles of Ni spinel ferrites. Accordingly, we examined in the present study the influence of Dy^{3+} doping on the structure, morphology, Mossbauer, ZFC-FC magnetization, and AC susceptibility of $NiDy_xFe_{2-x}O_4$ ($0.0 \leq x \leq 0.1$) nanoparticles. Various products were synthesized using a hydrothermal process.

2. Experimental

Various specimens with the chemical formula $NiDy_xFe_{2-x}O_4$ ($0.0 \leq x \leq 0.1$) have been prepared by a hydrothermal process. Analytical grade high purity chemical reagents including Dysprosium III nitrate hydrate ($Dy(NO_3)_3\ H_2O$), Nickel nitrate ($Ni(NO_3)_2\ 6H_2O$), Iron III nitrate ($Fe(NO_3)_3\ 9H_2O$), and Sodium Hydroxide (NaOH) were taken as starting materials. Then, the stoichiometric amount of these compositions was mixed in distilled water and the resulting mixture was left at room temperature.

Next, a clear solution was made for pH adjustment using 2M of NaOH solution and placed in a stainless steel-Teflon autoclave to initiate the hydrothermal treatment. Finally, the obtained sample was dried and grinded for further experimental analyses.

A Rigaku Benchtop Miniflex X-ray diffraction (XRD) diffractometer (Tokyo, Japan) with Cu K_α radiation at room temperature (RT) over a 2θ range from 20° to 70° was used for the structural analysis. Scanning electron microscopy (SEM, FEI Titan 80–300 kV FEG S/TEM, Hillsboro, OR, USA), along with energy dispersive X-ray spectroscopy (EDX) and transmission electron microscopy (TEM; FEI, Morgagni 268, Prague, Czech Republic), was used for the morphological and composition analyses. AC magnetic susceptibility, zero-field cooled (ZFC), and field cooled (FC) magnetization measurements were performed using a superconducting quantum interference device (PPMS DynaCool, Quantum Design, San Diego, CA, USA). ZFC-FC magnetizations were carried out at a temperature range of 2–400 K under a DC field of 100 Oe. Real and imaginary parts of AC susceptibility measurements were done at temperatures ranging from 350 to 2 K in the presence of an ac applied magnetic field of H_{ac} = 10 Oe and in different frequencies ranging from 50 to 10,000 Hz. Mössbauer spectra were performed at room temperature using a conventional Mössbauer spectrometer (Fast Com Tec PC-moss II, Oberhaching, Germany) under the constant acceleration mode using ^{57}Fe in an Rh matrix with an approximate activity of 10 m Ci. The speed scale and the velocity were calibrated using α-Fe and laser interferometry, respectively. The recorded spectra were analyzed and fit to the inbuilt Win-Normos fitting software (WISSEL company, Duisburg, Germany).

3. Results and Discussion

3.1. Structure

Figure 1 displays the XRD powder patterns of the studied $NiDy_xFe_{2-x}O_4$ ($0.0 \leq x \leq 0.1$) nanoparticles. Irrespective of Dy^{3+} contents, all the XRD peaks have been verified to the cubic nanosized Ni-spinel ferrites (JCPDS Card Number 54-0964), indicating the lattice site compatibility of the Dy^{3+} ions in the Ni spinel ferrite structure in the absence of any impurity. The calculated structural parameters of the prepared nanosized spinel ferrites were enlists in Table 1. It was realized that lattice parameters elongate due to the increase in the substitution contents and also show ionic radii disparity between Fe^{3+} (0.78 Å) and Dy^{3+} (1.03 Å). The calculated crystallite sizes (D_{XRD}) were in the range of 24 to 35 nm [16].

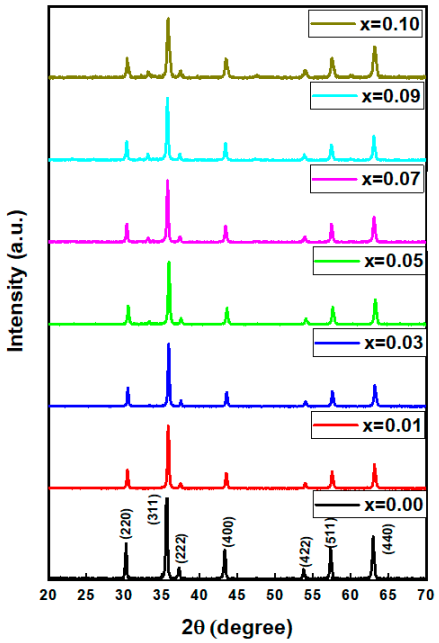

Figure 1. X-ray diffraction (XRD) powder patterns of prepared nanoparticles (NPs).

Table 1. Structural parameters of studied $NiDy_xFe_{2-x}O_4$ NPs.

x	a (Å)	V (Å^3)	D_{XRD} (nm)
0.00	8.3378	579.6451	34.7
0.01	8.3397	580.0333	33.1
0.03	8.3413	580.3630	34.7
0.05	8.3424	580.3463	30.8
0.07	8.3473	579.3824	32.3
0.09	8.3470	579.9142	33.1
0.10	8.3473	580.9998	24.3

3.2. Morphology

Figure 2 displays the SEM pictures, EDX spectra, and elemental mapping results for x = 0.01 and 0.05 samples. The surface morphology of these samples revealed a high degree of nanoparticle agglomeration. EDX analysis proved the existence of appropriate elements (Fe, Ni, Dy, and O) in the samples. Figure 3 illustrates the TEM image of the nanosized spinel ferrites containing Dy^{3+} contents of 0.05. The inset (Figure 3) displays the selected angle electron diffraction (SAED) patterns of the corresponding sample that confirmed the agglomeration of single crystalline Ni spinel ferrite nanoparticles.

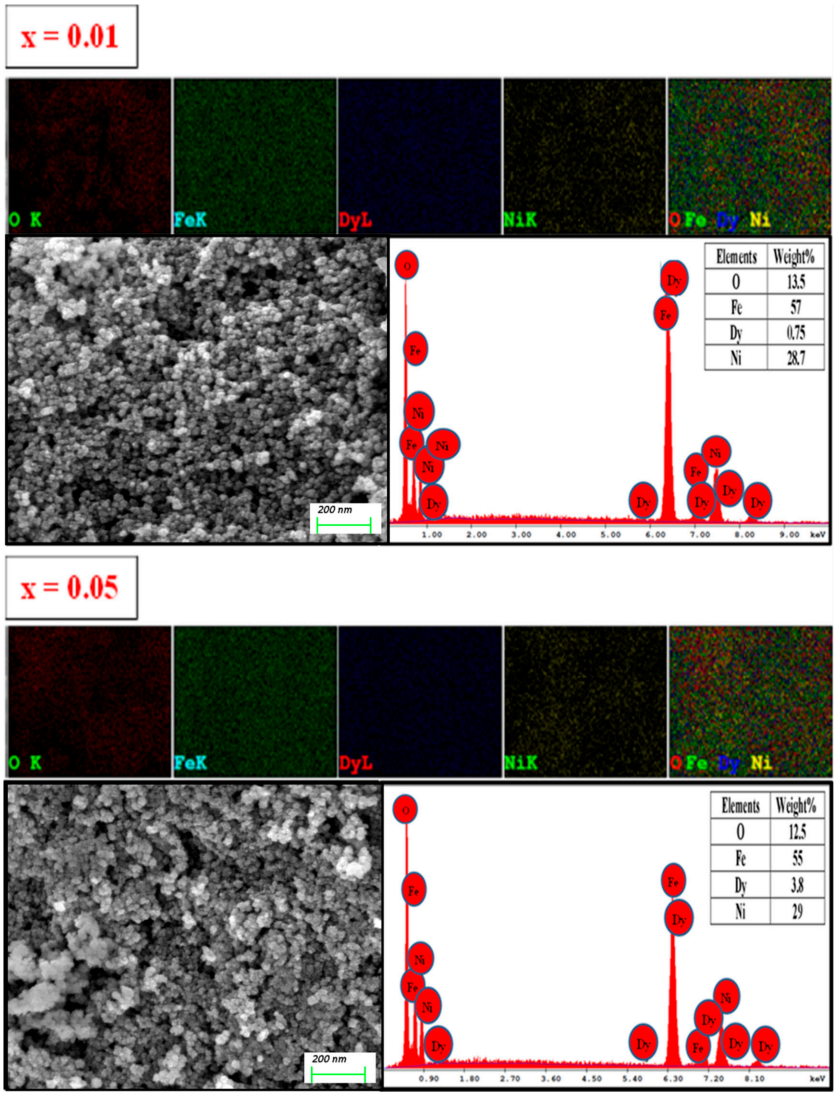

Figure 2. Elemental mapping, Scanning electron microscope (SEM) images and dispersive X-ray spectroscopy (EDX) of two selected x = 0.01 and 0.05 NPs.

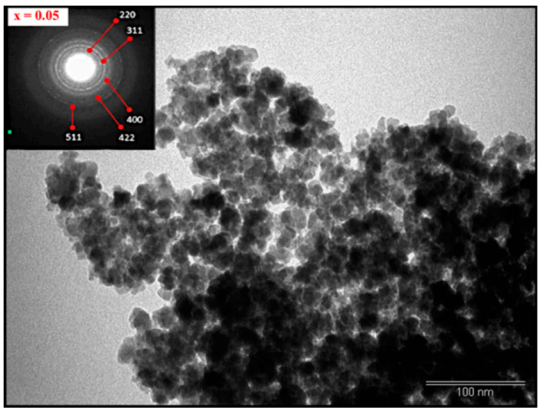

Figure 3. TEM image of selected $x = 0.05$ nanoferrite (Inset: corresponding selected angle electron diffraction (SAED) pattern).

3.3. Mössbauer Spectra

Figure 4 depicts the Mössbauer spectra of synthesized $NiDy_xFe_{2-x}O_4$ ($0.0 \leq x \leq 0.1$) NPs at room temperature. Table 2 enlists various Mössbauer parameters calculated by spectral fitting using three sextets (A for the tetrahedral sites and B and B_1 for the octahedral sites). Fe^{3+} ions in the tetrahedral A site are characterized by a large hyperfine field with an insignificant isomer shift. Conversely, the other two sextets with a comparatively smaller hyperfine field signify the occupation of Fe^{3+} at two dissimilar environments in the B-site [17]. Besides the ferromagnetic sextets, a minute paramagnetic doublet with quadrupole-splitting was evidenced for $NiDy_{0.01}Fe_{1.99}O_4$, $NiDy_{0.07}Fe_{1.93}O_4$, and $NiDy_{0.1}Fe_{1.9}O_4$ NPs. The occurrence of such a paramagnetic doublet was attributed to the fractions of Fe^{3+} with fewer nearest neighbors that possessed magnetically ordered spins. Interestingly, in the spinel ferrite structure, Fe^{3+} did not contribute to the super exchange interaction [18].

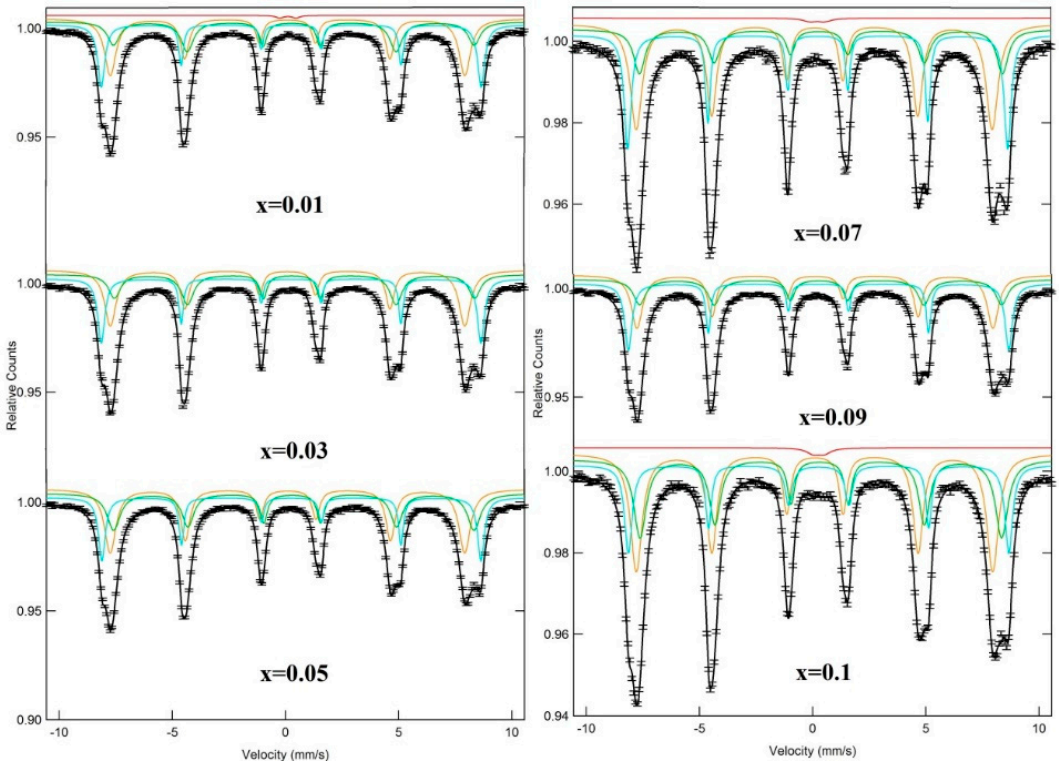

Figure 4. Mössbauer spectra of studied NPs.

Table 2. Evaluated Mössbauer parameters of studied ferrite NPs (B_{hf}: hyperfine magnetic field, I.S.: isomer shift, Q.S.: quadrupole splitting, W: line width, and R_A: Relative area).

x	Assignment of Sites	I.S. (±0.002) (mm/s)	Q.S. (±0.004) (mm/s)	B_{hf} (±0.02) (T)	W (±0.01) (mm/s)	R_A (%)	Cation Distribution
0.01	Sx-A: Fe^{3+}	0.368	0.005	52.045	0.218	17.298	$(Ni_{0.65}Fe_{0.35})_A$ $[Ni_{0.35}Dy_{0.01}Fe_{1.64}]_BO_4$
	Sx-B: Fe^{3+}	0.438	0.097	49.407	0.401	35.575	
	Sx-B_1: Fe^{3+}	0.202	0.011	48.566	0.37	46.375	
	Db: Fe^{+3+}	0.226	0.717	–	0.399	0.752	
0.03	Sx-A: Fe^{3+}	0.364	0	52.009	0.205	17.358	$(Ni_{0.66}Fe_{0.34})_A$ $[Ni_{0.34}Dy_{0.03}Fe_{1.63}]_BO_4$
	Sx-B: Fe^{3+}	0.455	0.119	49.337	0.383	34.389	
	Sx-B_1: Fe^{3+}	0.204	0.09	48.55	0.38	48.253	
0.05	Sx-A: Fe^{3+}	0.365	0.008	51.941	0.257	16.783	$(Ni_{0.67}Fe_{0.33})_A$ $[Ni_{0.33}Dy_{0.05}Fe_{1.62}]_BO_4$
	Sx-B: Fe^{3+}	0.438	0.071	49.379	0.395	35.528	
	Sx-B_1: Fe^{3+}	0.231	−0.018	48.559	0.402	47.689	
0.07	Sx-A: Fe^{3+}	0.366	−0.008	52.057	0.242	17.866	$(Ni_{0.65}Fe_{0.35})_A$ $[Ni_{0.35}Dy_{0.07}Fe_{1.58}]_BO_4$
	Sx-B: Fe^{3+}	0.464	0.072	49.737	0.466	25.675	
	Sx-B_1: Fe^{3+}	0.218	−0.023	48.76	0.422	54.952	
	Db: Fe^{3+}	0.345	0.625	–	0.725	1.5067	
0.09	Sx-A: Fe^{3+}	0.365	0.004	52.119	0.219	19.981	$(Ni_{0.62}Fe_{0.38})_A$ $[Ni_{0.38}Dy_{0.09}Fe_{1.53}]_BO_4$
	Sx-B: Fe^{3+}	0.424	0.066	49.614	0.445	35.589	
	Sx-B_1: Fe^{3+}	0.209	−0.005	48.766	0.394	45.43	
0.10	Sx-A: Fe^{3+}	0.37	−0.004	52.123	0.239	20.331	$(Ni_{0.6}Fe_{0.4})_A$ $[Ni_{0.4}Dy_{0.1}Fe_{1.5}]_BO_4$
	Sx-B: Fe^{3+}	0.441	0.053	49.544	0.397	31.53	
	Sx-B_1: Fe^{3+}	0.198	−0.02	48.825	0.413	46.22	
	Db: Fe^{3+}	0.379	0.481	–	0.696	1.9186	

The achieved relative area for the A and B sites clearly indicated the occupation of Ni^{3+} in the A and B sites. Kumar et al. acknowledged the preferential occupation of Dy^{3+} in the octahedral B sites of Co-ferrites [19,20]. Thus, the cation distribution in the proposed Dy^{3+} substituted nanoferrites was obtained following the formula unit of $(Ni_yFe_{1-y})_A$ $(Ni_{1-y}Dy_xFe_{1+y-x})_B$. The distribution of Fe^{3+} over the A and B sites was observed to be relative to the proportional area of A and B in the Mossbauer sub-spectra. Table 2 summarizes the approximate cation distribution obtained from the Mössbauer spectra. The results in Table 2 revealed that Fe^{3+} cations emigrated from the B site to A site due to Dy^{3+} substitution. The line width of the A site was randomly altered, whereas for B and B_1 sites, it was enhanced with the substitution of Fe^{3+} (0.64 Å) in the B sites by Dy^{3+} (0.91Å) having larger ionic radii than the former one. This observation authenticated the increase in the degree of disorder due to the substitution on B sites.

The values of the hyperfine magnetic fields for the A and B sites (Table 2) in the studied nanosized spinel ferrites were first reduced with an increase in Dy^{3+} contents up to 0.05 and then enhanced at 0.07. Eventually, the hyperfine field for A site was continuously enhanced, but for the B site it was diminished. This alteration in the hyperfine field for the A and B sites was attributed to the addition of the diamagnetic Dy^{3+} that replaced the ferromagnetic Fe^{3+} with a higher magnetic moment (5 μ_B) and lowered the average number of magnetic linkages ($Fe_A^{3+} - O - Fe_B^{3+}$). Thus, Fe^{3+} nuclei experienced a reduction in the magnetic field at both the sublattices up to the Dy3+ content of 0.05. Beyond 0.05, the number of Fe^{3+} at the A site was augmented, thereby increasing the hyperfine magnetic field and magnetic moment of Fe^{3+} at the A site.

3.4. ZFC-FC Magnetizations

Figure 5 shows the curves of zero-field-cooled (ZFC) and field-cooled (FC) temperature dependencies of the magnetization, M_{ZFC} (T) and M_{FC} (T), of $NiFe_{2-x}Dy_xO_4$ (where x = 0.00, 0.03 and 0.09) NPs. These measurements were performed in a temperature interval ranging between 2 and 400 K under a DC field of 100 Oe. For M_{ZFC} (T) measurements, the sample was cooled, first of all, from room temperature (RT) to a very low temperature in the absence of an applied field and subsequently the magnetization was recorded by increasing the temperature in the presence of the field. However, in the M_{FC} (T) measurements, the magnetization was recorded by cooling the product in the presence of applied field. A splitting and a large irreversibility between M_{ZF} (T) and M_{FC} (T) curves for different synthesized products can be clearly seen in Figure 5. The M_{FC} (T) increased gradually and remained constant below temperature T_s, while the M_{ZFC} (T) decreased with a lowering of the temperature down to about 4 K. The dispersion of M_{ZFC}-M_{FC} versus T curves is congruent with the poly-disperse character of magnetic NPs, with a correlated distribution in particle size and individual anisotropy axes [21]. The enlargement could also owe to dipolar interactions among particles [21].

It is reported in the literature that the manifestation of a peak in the M_{ZFC} (T) plots is associated to the blocking temperature (T_B) [22]. The curves of M_{ZFC} (T) of the prepared products showed an incomplete maximum or broad maximum at around the temperature noted T_B. This is typical for superparamagnet (SPM) materials, which show the properties of classical paramagnet materials (PM) above T_B, where the total spin is equal to the spin of a whole NPs but behave as ferromagnetic (FM) materials below their blocking temperature (T_B). Below T_B, the M_{FC} (T) and M_{ZFC} (T) curves considerably diverge, and the various ferrite NPs are in the FM state (blocked state). Above T_B, the M_{FC} (T) and M_{ZFC} (T) curves coincide, which is because all NPs are in the same SPM state. At $T = T_B$, the thermal activation overcomes the magnetic anisotropy barrier, which leads to fluctuations in magnetization [23]. Therefore, the wide peak at T_B in the M_{ZFC} (T) curves is an indication of a broadened energy barrier distribution. Further, it can be seen that the blocking temperature varies by increasing Dy substitution content. The non-substituted product $NiFe_2O_4$ shows a blocking temperature around $T_B \approx 390$ K. The x = 0.03 product exhibits a well-defined T_B at around 300 K. By further increasing the amount of Dy, the product synthesized with x = 0.09 was not able to reach the T_B within 400 K, so the T_B value is superior than 400 K for x = 0.09. It can be seen clearly that the blocking temperature decreases

for a lower Dy content (x = 0.03) and then increases for higher content (x = 0.09). The dependence of the T_B on particles size has been reported in previous studies [24]. The lower T_B is attributed to smaller particle size or narrow size distribution. However, the higher T_B represents a larger particle size. Nevertheless, the different x = 0.00, 0.03 and 0.09 products show approximately same particles size. Therefore, the variations in blocking temperature with substitution effects are not predominantly influenced by the grain size. Thus, in addition to the particle size effect, the T_B could also be affected by numerous other extrinsic factors, mostly related to interactions among particles and intrinsic factors that principally include a magneto–crystalline, surface and shape anisotropy [22,25]. We noticed in the synthesized product with x = 0.03 that the M_{ZFC} (T) exhibits a breaking at temperatures indicated by the dashed circle in Figure 5.

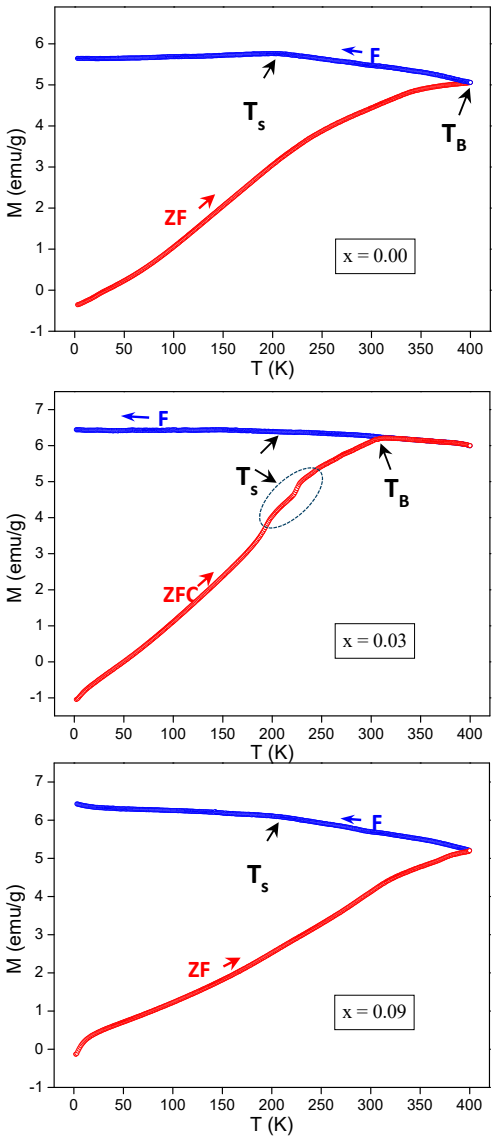

Figure 5. M_{ZFC} (T) and M_{FC} (T) curves of the three selected NPs.

On the other hand, the M_{FC} (T) curves increase smoothly for different samples with a decrease of temperature, while a kind of saturation in the magnetization is noticed below the temperature noted by T_s for all samples. It is reported in the literature that for SPM nanoparticles, the curve of M_{FC} (T) increases continuously [26,27]. Nevertheless, in the case of super-spin glass (SSG) systems in which the interactions among particles are strong, a flat type or a slow increase is observed [26,27].

Therefore, the detected flat nature below T_s in the M_{FC} (T) curves establishes the occurrence of an SSG-like state. The origin of the observed magnetic features in ZFC-FC magnetization part will be discussed in detail in the analyses of the AC susceptibility measurements. The latter are a useful way to identify the freezing dynamics of the spin-glass (SG) materials.

3.5. AC Susceptibility

For measurements of AC susceptibility (χ_{ac}), an AC magnetic field (H_{ac}) is applied to the sample and, as a consequence, a resultant magnetic moment is measured. The χ_{ac} is represented as follows:

$$\chi_{ac} = \chi' + i\chi''$$

where χ' real and χ'' imaginary parts are, respectively, the in-phase and out-phase components of χ_{ac}. It should be noted that the relaxation time (τ) of the AC susceptibility measurement is not based upon the energy barrier ($E_a = K_{eff}V$ where K_{eff} is the effective anisotropy constant and V is the volume of particles). However, it is influenced by the external excitation frequency. The AC susceptibility measurements give important details about the dynamics of the systems and the strength of exchange interactions between the magnetic nano-particles (MNPs) and between the different cations.

Firstly, we will discuss the χ' real part measurements of the two NPs samples with x = 0.00 and 0.03. Figure 6 presents the curves of χ'versus T, ranging from 350 to 2 K, for x = 0.00 and 0.03 products, performed in the presence of an H_{ac} = 10 Oe and in a frequency range of 50–10^4 Hz. The magnitude of χ' for x = 0.03 increased slightly compared to the non-substituted product (x = 0.00), which is in accordance with M_{ZFC} (T) and M_{FC} (T) measurements. The in-phase AC susceptibility data of the different samples showed dispersion and a decrease in magnitude while increasing the applied frequency from 50 Hz to 10 kHz. The $\chi'(T)$ curve of the non-substituted $NiFe_2O_4$ NPs exhibited a peak at around 300 K. However, the x = 0.03 product did not show any peak up to 350 K.

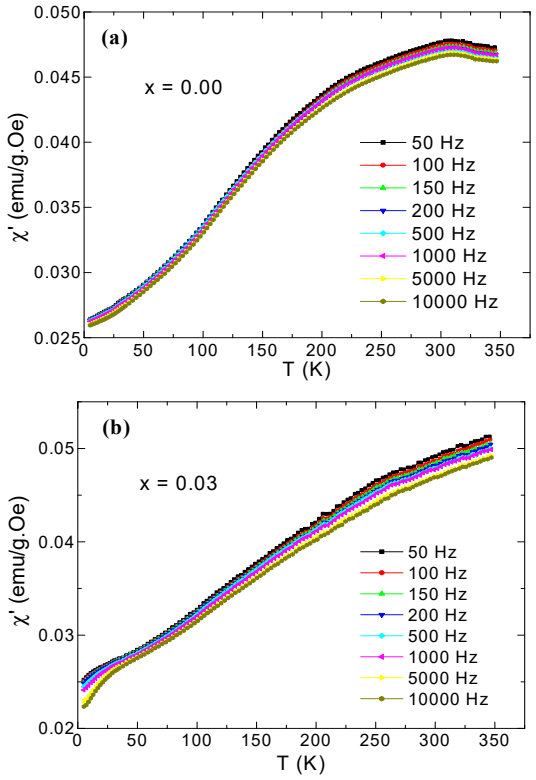

Figure 6. $\chi'(T)$ curves of the prepared (**a**) $NiFe_2O_4$ and (**b**) $NiFe_{1.97}Dy_{0.03}O_4$ NPs.

Figure 7 shows the $\chi''(T)$ curves for $NiFe_{2-x}Dy_xO_4$ (where x = 0.00 and 0.03) performed in a H_{ac} = 10 Oe and in the frequency range of 50–10^4 Hz. It can be seen that both samples display two peaks—the first at the higher temperature indicated by T_B in the figure, which is associated with magnetic blocking of huge core spins, and the second indicated by T_s, which can be associated with the spin-glass freezing on the surface of a single NP [28]. The $\chi'(T)$ curves do not offer any information about these two peaks, hence from now on we will focus only on analyses of $\chi''(T)$ curves.

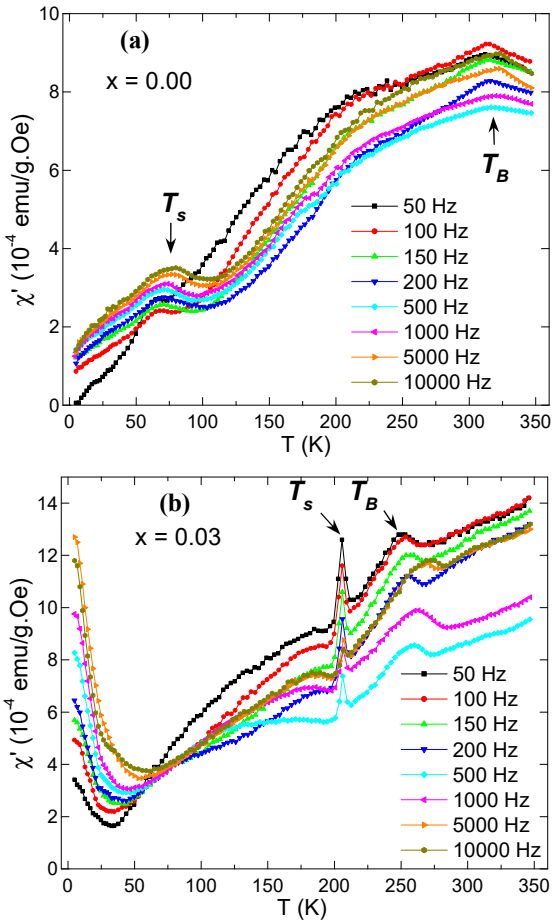

Figure 7. $\chi''(T)$ curves for (**a**) $NiFe_2O_4$ and (**b**) $NiFe_{1.97}Dy_{0.03}O_4$ NPs.

At the same applied frequency, the T_B and T_s shifted to lower temperatures with Dy substitution compared to the non-substituted one. This is consistent with the M_{ZFC} analyses. Both the blocking temperature T_B and spin-glass freezing temperature T_s are affected by frequency. Both show a shift to higher temperatures upon increasing the value of the applied frequency (f). Similar behavior is observed in the spin-frustrated system of $CoFe_2O_4$ NPs dispersed in an SiO_2 matrix [28]. The shifting with f is helpful for evaluating dynamic magnetic behaviors, deducing the anisotropic energy, the magnetic anisotropy, and the interaction strength between MNPs.

Various physical laws can be used to investigate the f-dependence shift of T_B and T_s temperatures. The Neel–Arrhenius (N–A) law was first tested to fit the experimental data (Figure 8). This theory is valid for thermal excitations of non-interacting single-barrier NPs and is expressed as follows [29,30]:

$$\tau = \tau_o \, exp(E_a/k_B T)$$

where $\tau = 1/f$ is the measured time, τ_0 is the jump attempt time (in the range of 10^{-9}–10^{-13} s), k_B is the Boltzmann constant, and $E_a = K_{eff}V$ is the activation energy barrier. The estimated values of $\tau_0 = 1/f_0$, E_a/k_B and K_{eff} for different samples are given in Table 3. The best N–A fit offers very

unreasonable values for τ_0 and E_a/k_B. This indicates that the synthesized products do not obey the thermally activated N–A law and, as a consequence, they are non-interacting.

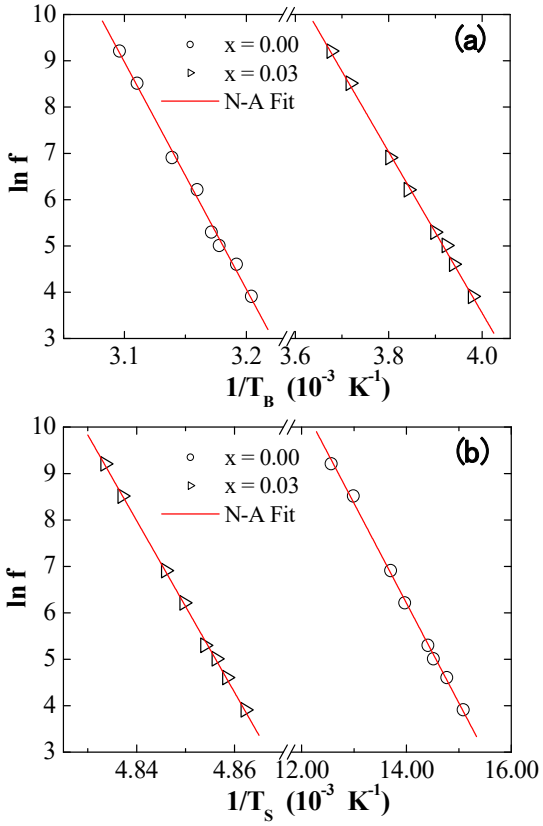

Figure 8. Plots of (**a**) $\ln(f)$ versus $1/T_B$ and (**b**) $\ln(f)$ versus $1/T_s$ for two selected $NiFe_{2-x}Dy_xO_4$ NPs where x = 0.00 and 0.03 fit to the Neel–Arrhenius (N–A law) (solid lines).

Table 3. Fitting parameters (τ_o, E_0/k_B and) of prepared $NiFe_{2-x}Dy_xO_4$ (x = 0.00 and 0.03) NPs estimated using different laws.

Models	Parameters	Values			
		Peak (T_B)		Peak (T_S)	
		x = 0.00	x = 0.03	x = 0.00	x = 0.03
Neel–Arrhenius	τ_o (s)	1.05×10^{-70}	1.68×10^{-32}	1.69×10^{-16}	1.26×10^{-392}
	E_0/k_B (K)	49,083	17,403	2150	184,793
	K_{eff} (erg/cm^3)	3.09×10^5	1.09×10^5	1.35×10^4	1.16×10^6
Vogel–Fulcher	τ_o (s)	5.45×10^{-10}	1.32×10^{-9}	8.00×10^{-7}	6.06×10^{-46}
	E_0/k_B (K)	367.57	621.53	100.38	2188.95
	T_o (K)	292.71	216.76	58.82	183.84
	K_{eff} (erg/cm^3)	2.32×10^3	3.92×10^3	6.34×10^2	1.38×10^4
Critical slowing down	τ_o (s)	****	****	2.88×10^{-9}	2.50×10^{-12}
	T_g (K)	****	****	58.39	205.55
	$z\nu$	****	****	5.77	3.95

The Vogel–Fulcher (V–F) law is a useful model for investigating the interactions between NPs. This law uses an additional parameter, T_0, that represents the strength of inter-particle interactions. Based on this model, the relaxation is described as follows [29,30]:

$$\tau = \tau_o \exp[E_a/k_B(T - T_0)].$$

The fitting data using the V–F law of the plots of f vs. T_B and f vs. T_s for the prepared products are illustrated in Figure 9a,b, respectively. The different estimated parameters are summarized in Table 3. The analysis of f-dependent T_B now gives reasonable τ_0 and E_a/k_B values. Obviously, the T_0 values are not negligible compared to T_B. The occurrence of T_0 confirms the presence of moderate inter-particle interactions between the NPs [28–30]. It is found, moreover, that τ_0 increased more for the x = 0.03 product than for the x = 0.00 one. The increase in the τ_0 for x = 0.03 product suggests the strengthening of interactions between NPs [29,30]. Compared to the x = 0.00 product, the values of E_a/k_B and K_{eff} improved with Dy substitution for x = 0.03. This improvement iresulted from the strengthening of magnetic interactions among different NPs and the increase of magnetic anisotropy sources [29,30].

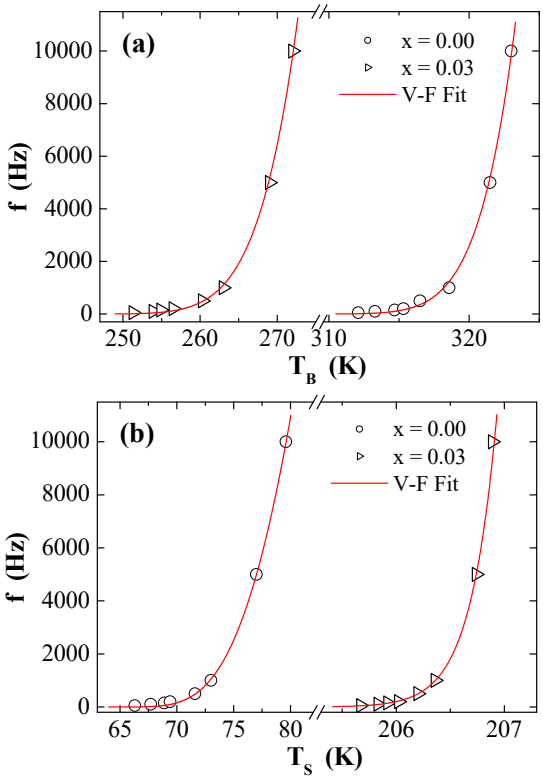

Figure 9. Plots of (**a**) f versus T_B and (**b**) f versus T_s for $NiFe_{2-x}Dy_xO_4$ (x = 0.00 and 0.03) NPs (solid lines present the Vogel–Fulcher (V–F) fit).

In other hand, the investigation of f vs. T_s provides unphysical values for τ_0. Therefore, the critical slowing down (CSD) law is used to study the presence of SG behavior in the synthesized NPs. Based on this model, the relaxation is expressed as [30]:

$$\tau = \tau_0^* \left[\frac{T_s}{T_g} - 1 \right]^{-(z\upsilon)}$$

where τ_0^* is associated to the coherence time of coupled individual "atomic" spins in the NP (in the range 10^{-6}–10^{-13} s) [31], T_g is the SG freezing temperature, and T_s is the f-dependent freezing temperature. The "$z\upsilon$" is the critical exponent that offers information about the SG, and it varies from 4 to 12 for various SG systems [28]. We fit the same f vs. T_s data using the CSD law, in order to examine the possibility of the SG nature (Figure 10). The various deduced parameters are listed in Table 3. The obtained reasonable values of τ_0, T_g and "$z\upsilon$" proved the existence of SG behavior in the prepared samples. Similar comportment has been reported in numerous products, such as $CoFe_2O_4/(SiO_2)_x$ systems [28], Fe_3O_4 MNPs ($z\upsilon$ = 8.2 and $\tau \sim 10^{-9}$ s) [32,33], soft ferrite $Ni_{0.3}Zn_{0.7}Fe_2O_4$ NPs ($z\upsilon$ = 8.01

and $\tau \sim 10^{-12}$ *s*) [34], and $La_{0.9}Sr_{0.1}MnO_3$ NPs [35]. It is reported that the strength of magnetic interactions increases based on the decreasing "zv" exponent. The non-substituted $NiFe_2O_4$ product exhibits a "zv" value equal to 5.11, and it decreases to 3.95 with Dy substitution for $x = 0.03$. This result indicates the improvement of the magnetic interactions among NPs for the $x = 0.03$ product.

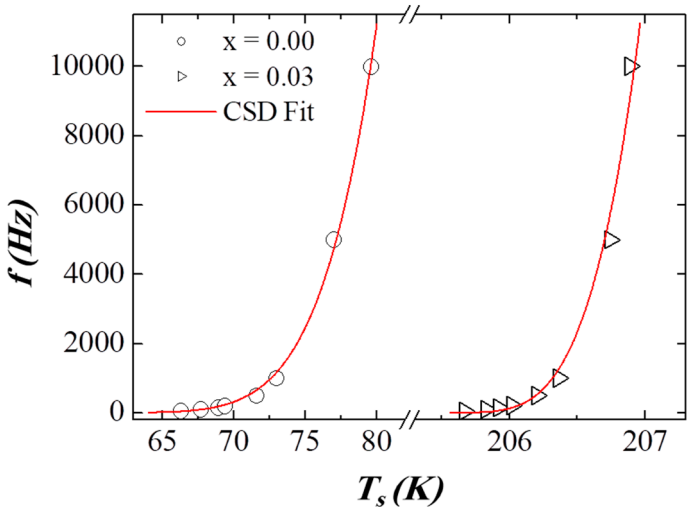

Figure 10. Plots of f versus T_s for the two selected $x = 0.00$ and 0.03 NPs. The solid lines represent the critical slowing down (CSD) fit.

4. Conclusions

Series of Dy^{3+} doped ferrite nanoparticles of $NiFe_{2-x}Dy_xO_4$ ($0.0 \leq x \leq 0.1$) NPs were prepared using a hydrothermal method. The as-prepared specimens were thoroughly characterized using various analytical measurement techniques to determine their structure, morphology, and distinct magnetic traits. An XRD pattern of nanoferrites confirmed the formation of a spinel cubic structure. The Mössbauer spectra displayed the cation distribution, verifying the occupation of Dy^{3+} ions at octahedral B sites. The measurements of ZFC-FC magnetization and AC susceptibility were examined. The magnetic data showed the existence of two critical temperatures. The first one is the blocking temperature T_B, which corresponds to the magnetic blocking of huge core spins, and the second is T_s, which can be associated to spin-glass freezing arising on the surface of a single NP. The T_B and T_s temperatures vary with the Dy substitution. This is due to numerous intrinsic and extrinsic factors that principally include magneto-crystalline factors, interactions among particles, surface, and shape anisotropy. Furthermore, both the T_B and T_s temperatures are affected by applied frequency. Various physical laws, such as Neel-Arrhenius, Vogel-Fulcher, and critical slowing down, are used to investigate the f-dependence shift of the T_B and T_s temperatures. It was found that the Dy substitution enhances the magnetic interactions. Compared to the $x = 0.00$ product, the E_a/k_B and K_{eff} values improved for $x = 0.03$. This proved that the magnetic interactions are enhanced due to the Dy substitution.

Author Contributions: Synthesis of the sample (M.A.A., Y.S. and A.B.). XRD investigation and analysis (M.A.A. and A.B.). Investigation and writing of the ZFC-FC magnetization and AC susceptibility (Y.S.). Investigation and analysis of the Mossbauer spectra (H.G.). Participation in drafting the article or revising it critically for important intellectual content (S.A., A.M., I.E. and A.V.T). Supervision, review, and editing (M.A.A., Y.S. and A.B.).

Funding: The authors highly acknowledge the Institute for Research & Medical Consultations (Projects application No. 2017-IRMC-S-3; No. 2018-IRMC-S-1 and No. 2018-IRMC-S-2) and the Deanship for Scientific Research (Projects application No. 2017-576-IRMC and No. 2018-209-IRMC) of Imam Abdulrahman Bin Faisal University (Saudi Arabia) for supporting this study.

Acknowledgments: The authors thank the Institute for Research & Medical Consultations (IRMC) of Imam Abdulrahman Bin Faisal University (IAU—Saudi Arabia) for the supports. The technical assistance provided by Core Labs of King Abdullah University of Science and Technology (KAUST) is highly appreciated.

Conflicts of Interest: The authors declare no conflict of interest.

References

1. Kavas, H.; Kasapoğlu, N.; Baykal, A.; Köseoğlu, Y. Characterization of NiFe2O4 nanoparticles synthesized by various methods. *Chem. Pap.* **2009**, *63*, 450–455. [CrossRef]
2. Ati, A.A.; Othaman, Z.; Samavati, A. Influence of cobalt on structural and magnetic properties of nickel ferrite nanoparticles. *J. Mol. Struct.* **2013**, *1052*, 177–182. [CrossRef]
3. Vigneswari, T.; Raji, P. Structural and magnetic properties of calcium doped nickel ferrite nanoparticles by co-precipitation method. *J. Mol. Struct.* **2017**, *1127*, 515–521. [CrossRef]
4. Wahba, A.M.; Mohamed, M.B. Structural, magnetic, and dielectric properties of nanocrystalline Cr-substituted $Co_{0.8}Ni_{0.2}Fe_2O_4$ ferrite. *Ceram. Int.* **2014**, *40*, 6127–6135. [CrossRef]
5. Sözeri, H.; Alveroğlu, E.; Kurtan, U.; Şenel, M.; Baykal, A. Cobalt substituted nickel ferrites via Pechini's sol–gel citrate route: X-band electromagnetic characterization. *J. Supercond. Nov. Magn.* **2013**, *26*, 213–218.
6. Mozaffari, M.; Amighian, J.; Darsheshdar, E. Magnetic and structural studies of nickel-substituted cobalt ferrite nanoparticles, synthesized by the sol–gel method. *J. Magn. Magn. Mater.* **2014**, *350*, 19–22. [CrossRef]
7. Yaseneva, P.; Bowker, M.; Hutchings, G. Structural and magnetic properties of Zn-substituted cobalt ferrites prepared by co-precipitation method. *Phys. Chem. Chem. Phys.* **2011**, *13*, 18609. [CrossRef] [PubMed]
8. Srinivasamurthy, K.; Angadi, V.; Kubrin, S.; Matteppanavar, S.; Kumar, P.M.; Rudraswamy, B. Evidence of enhanced ferromagnetic nature and hyperfine interaction studies of Ce-Sm doped Co-Ni ferrite nanoparticles for microphone applications. *Ceram. Int.* **2018**, *44*, 18878–18885. [CrossRef]
9. Stergiou, C. Magnetic, dielectric and microwave absorption properties of rare earth doped Ni–Co and Ni–Co–Zn spinel ferrites. *J. Magn. Magn. Mater.* **2017**, *426*, 629–635. [CrossRef]
10. Boda, N.; Boda, G.; Naidu, K.C.B.; Srinivas, M.; Batoo, K.M.; Ravinder, D.; Reddy, A.P. Effect of rare earth elements on low temperature magnetic properties of Ni and Co-ferrite nanoparticles. *J. Magn. Magn. Mater.* **2019**, *473*, 228–235. [CrossRef]
11. Singh, R.K.; Shah, J.; Kotnala, R. Magnetic and dielectric properties of rare earth substituted $Ni_{0.5}Zn_{0.5}Fe_{1.95}R_{0.05}O_4$ (R = Pr, Sm and La) ferrite nanoparticles. *Mater. Sci. Eng. B* **2016**, *210*, 64–69. [CrossRef]
12. Akhtar, M.N.; Khan, M.A. Effect of rare earth doping on the structural and magnetic features of nanocrystalline spinel ferrites prepared via sol gel route. *J. Magn. Magn. Mater.* **2018**, *460*, 268–277. [CrossRef]
13. Sahariya, J.; Mund, H.S.; Sharma, A.; Dashora, A.; Itou, M.; Sakurai, Y.; Ahuja, B.L. Magnetic properties of $NiFe_{2-x}RE_xO_4$ (RE=Dy, Gd) using magnetic Compton scattering. *J. Magn. Magn. Mater.* **2014**, *360*, 113–117. [CrossRef]
14. Bharathi, K.K.; Noor-A-Alam, M.; Vemuri, R.; Ramana, C.V. Correlation between microstructure, electrical and optical properties of nanocrystalline $NiFe_{1.925}$ $Dy_{0.075}$ O_4 thin films. *RSC Adv.* **2012**, *2*, 941–948. [CrossRef]
15. Almessiere, M.; Slimani, Y.; Güner, S.; Baykal, A.; Ercan, I. Effect of dysprosium substitution on magnetic and structural properties of $NiFe_2O_4$ nanoparticles. *J. Rare Earths* **2019**. [CrossRef]
16. Chawla, S.K.; Meena, S.S.; Kaur, P.; Mudsainiyan, R.K.; Yusuf, S.M. Effect of site preferences on structural and magnetic switching Properties of Co–Zr doped strontium hexaferrite $SrCo_xZr_xFe_{(12-2x)}O_{19}$. *J. Magn. Magn. Mater.* **2015**, *378*, 84–91. [CrossRef]
17. Joseyphus, R.J.; Narayanasamy, A.; Shinoda, K.; Jeyadevan, B.; Tohji, K. Synthesis and magnetic properties of the size-controlled Mn–Zn ferrite nanoparticles by oxidation method. *J. Phys. Chem. Solids* **2006**, *67*, 1510–1517. [CrossRef]
18. Chae, K.P.; Kwon, W.H.; Lee, J.-G. Influence of aluminum doping in Li–Co–Ti ferrite. *J. Magn. Magn. Mater.* **2012**, *324*, 2701–2705. [CrossRef]
19. Kumar, H.; Sing, J.P.; Srivastava, R.C.; Patel, K.R.; Chae, K.H. Synthesis and characterization of $Dy_xCoFe_{2-x}O_4$ nanoparticles. *Superlattices Microstruct.* **2017**, *109*, 296–306. [CrossRef]

20. Kumar, H.; Srivastava, R.; Singh, J.P.; Negi, P.; Agrawal, H.; Das, D.; Chae, K.H. Structural and magnetic study of dysprosium substituted cobalt ferrite nanoparticles. *J. Magn. Magn. Mater.* **2016**, *401*, 16–21. [CrossRef]
21. Morales, M.-B.; Phan, M.-H.; Pal, S.; Frey, N.-A.; Srikanth, H. Particle blocking and carrier fluid freezing effects on the magnetic properties of Fe_3O_4-based ferrofluids. *J. Appl. Phys.* **2009**, *105*, 07B511. [CrossRef]
22. Humbe, A.V.; Kounsalye, J.S.; Shisode, M.V.; Jadhav, K. Rietveld refinement, morphology and superparamagnetism of nanocrystalline $Ni_{0.70-x}Cu_xZn_{0.30}Fe_2O_4$ spinel ferrite. *Ceram. Int.* **2018**, *44*, 5466–5472. [CrossRef]
23. Graham, C.D. *Introduction to Magnetic Materials*; Wiley: Hoboken, NJ, USA, 2009.
24. Bhowmik, R.; Aneeshkumar, K. Low temperature ferromagnetic properties, magnetic field induced spin order and random spin freezing effect in $Ni_{1.5}Fe_{1.5}O_4$ ferrite; prepared at different pH values and annealing temperatures. *J. Magn. Magn. Mater.* **2018**, *460*, 177–187. [CrossRef]
25. Ajroudi, L.; Mliki, N.; Bessais, L.; Madigou, V.; Villain, S.; Leroux, C.; Leroux, C. Magnetic, electric and thermal properties of cobalt ferrite nanoparticles. *Mater. Res. Bull.* **2014**, *59*, 49–58. [CrossRef]
26. Peddis, D.; Cannas, C.; Piccaluga, G.; Agostinelli, E.; Fiorani, D. Surface spin freezing effects on enhanced saturation magnetization and magnetic anisotropy in $CoFe_2O_4$ nanoparticles. *Nanotechnology* **2010**, *21*, 125705. [CrossRef]
27. Chen, X.; Bedanta, S.; Petracic, O.; Kleemann, W.; Sahoo, S.; Cardoso, S.; Freitas, P.P.; Freitas, P. Superparamagnetism versus superspin glass behavior in dilute magnetic nanoparticle systems. *Physica B* **2005**, *72*, 214436. [CrossRef]
28. Zeb, F.; Sarwer, W.; Nadeem, K.; Kamran, M.; Mumtaz, M.; Krenn, H.; Letofsky-Papst, I. Surface spin-glass in cobalt ferrite nanoparticles dispersed in silica matrix. *J. Magn. Magn. Mater.* **2016**, *407*, 241–246. [CrossRef]
29. Almessiere, M.A.; Slimani, Y.; Güngüneş, H.; Baykal, A.; Trukhanov, S.V.; Trukhanov, A.V. Manganese/Yttrium Codoped Strontium Nanohexaferrites: Evaluation of Magnetic Susceptibility and Mossbauer Spectra. *Nanomaterials* **2019**, *9*, 24. [CrossRef]
30. Slimani, Y.; Almessiere, M.; Baykal, A. AC susceptibility study of Cu substituted $BaFe_{12}O_{19}$ nanohexaferrites. *Ceram. Int.* **2018**, *44*, 13097–13105. [CrossRef]
31. Kumar, D.; Banerjee, A. A critical examination of magnetic states of $La_{0.5}Ba_{0.5}CoO_3$: Non-Griffiths phase and interacting ferromagnetic-clusters. *arXiv* **2012**, arXiv:1211.4936.
32. Suzuki, M.; Fullem, S.I.; Suzuki, I.S.; Wang, L.; Zhong, C.-J. Observation of superspin-glass behavior inFe3O4nanoparticles. *Phys. B* **2009**, *79*, 024418. [CrossRef]
33. Fiorani, D.; Testa, A.M.; Lucari, F.; D'Orazio, F.; Romero, H. Magnetic properties of maghemite nanoparticle systems: Surface anisotropy and interparticle interaction effects. *B: Condens. Matter* **2002**, *320*, 122–126. [CrossRef]
34. Rahimi, M.; Kameli, P.; Ranjbar, M.; Salamati, H. The effect of polyvinyl alcohol (PVA) coating on structural, magnetic properties and spin dynamics of $Ni_{0.3}Zn_{0.7}Fe_2O_4$ ferrite nanoparticles. *J. Magn. Magn. Mater.* **2013**, *347*, 139–145. [CrossRef]
35. Eshraghi, M.; Kameli, P. Structural and Magnetic Properties of La0.9Sr0.1MnO3 Micro and Nanometer-Sized Manganite Samples. *J. Mater. Sci.* **2014**, *3*, 1.